Title: Induced Membrane Curvature Bypasses Clathrin's Essential Endocytic Function

Authors: Robert C Cail[1], Cyna R Shirazinejad[1], and David G Drubin[1,2] *

Affiliations:

[1]Biophysics Graduate Group, University of California Berkeley; Berkeley, CA, 94720-3202, USA.

[2]Department of Molecular and Cell Biology, University of California Berkeley; Berkeley, CA, 94720-3202, USA.

*Corresponding author. Email: drubin@berkeley.edu

Abstract: During clathrin-mediated endocytosis (CME), flat plasma membrane is rapidly remodeled to produce a nanometer-scale spherical vesicle. The mechanisms underlying this shape change are not known, but it has been hypothesized that the clathrin coat stabilizes membrane curvature. Here, we used nanopatterning to produce glass-like substrates with U-shaped features mimicking membrane shapes induced by fibrillar materials such as collagen. These substrates bend the ventral plasma membranes of cells grown on them into shapes characteristic of the energetically-unfavorable U-shaped intermediate stage of CME. This induced plasma membrane curvature recruits the endocytic machinery, enhances endocytic site maturation, and partially bypasses clathrin's role in CME, supporting the conclusion that clathrin's essential endocytic function is to stabilize membrane curvature.

One-Sentence Summary: The physical cue of nanometer-scale curvature creates endocytic vesicles in human cells, even without the protein clathrin.

Main Text: Cells grow and migrate in complex 3D environments, wherein nanoscale membrane bending is induced by both external environmental factors and intrinsic cellular processes: constraints outside the cell, such as the extracellular matrix (ECM) and cell-cell junctions, force the cell to adopt particular geometries, and intracellular processes like endocytic vesicle formation reshape the membrane from within (*1–3*). Clathrin-mediated endocytosis (CME) is a constitutive membrane-bending process that regulates a wide array of cellular functions including cell adhesion and migration (*4*, *5*). To generate vesicles, CME first bends the plasma membrane into a clathrin-coated pit (CCP). CCPs localize preferentially to sites of nanoscale curvature in cultured cells (*6*, *7*), suggesting that induced plasma membrane geometry may play a physiological role in CCP nucleation and dynamics.

Clathrin is essential for productive CME; upon clathrin disruption through siRNA or chemical inhibition, CCPs stall as protein aggregates with shallow curvature (*8*, *9*). However, clathrin can adopt distinct functional conformations including the spherical cage, flat plaque, and tubular lattice (*7*, *10-11*). This conformational flexibility and variability have led to debate about clathrin's activity during CME: what role does clathrin play in membrane budding, given its affinity for membranes of distinct curvatures? How does the 3-dimensional structure of the cellular environment, which alters membrane geometry, influence CCP formation and kinetics? Answering these questions promises to provide new insights into how productive CCPs are formed, and into CME's membrane curvature-generating mechanism. By creating

nanofabricated ridges that induce a range of nanoscale membrane curvatures by mimicking ECM fibers across the ventral cell membrane, we set out to answer these questions.

Ormocomp nanoridges induce membrane curvature and recruit the endocytic machinery

To induce membrane curvature across nanometer-range size scales, we applied a low-cost, high-throughput nanofabrication method termed UV-Nanoimprint Lithography (UV-NIL) (*12*) (Fig 1A). We selected the organic/inorganic hybrid material Ormocomp as our substrate because of the near-exact match of its refractive index to that of borosilicate glass, allowing us to conduct Total Internal Reflection Fluorescence (TIRF) microscopy, a standard imaging method in the CME field (*13*). To produce substrates through UV-NIL, we first created a mold through electron-beam lithography and reactive-ion etching on a silicon wafer (*14*) (Fig S1A). This mold features mm-long, cylindrical invaginations spaced at a pitch of 2 μm, with widths of 75, 120, 200, 300, 500, and 1000 nm (Fig 1B). The depth of an invagination varies from 200 to 300 nm. This mold served as the basis for Ormocomp substrate production. The resulting Ormocomp substrates bear the inverse geometry of the mold and therefore have cylindrical protrusions, which we term nanoridges (Fig 1B).

Upon exposure to intense UV irradiation, Ormocomp polymerizes through polyacrylate chemistry (Fig S1A). Ormocomp substrate manufacturing requires only ~15 minutes per substrate, allowing for replicated experiments and wider screening of conditions than is possible with slower nanofabrication processes.

To determine how the nanoridges affect plasma membrane shape, we seeded MDA-MB-231 cells on nanoridge substrates and performed thin-section TEM of substrate-grown cells. Electron

micrographs revealed that the plasma membrane bends around nanoridges of different diameters (Fig 1C). By measuring the diameter of multiple ridge-membrane interfaces across >3 cells per ridge size, we found that the nanoridges induce consistent membrane diameter as a function of ridge size (Fig 1D). The smallest nanoridge, 75 nanometers, induced a membrane diameter of ~142 nm, approximately 50% larger than the diameter of a fully-formed vesicle, with a linear increase up to the 500 nm ridge, which induced ~650 nm diameter curvature. The shape of the membrane bent around nanoridges was similar to the shapes seen in MDA-MB-231 cell membranes wrapped around collagen fibers, which are known to induce clathrin structures known as Tubular Clathrin/AP2 Lattices (TCALs) (*7*). When cells expressing RFP-tagged AP2, an early-arriving CME protein, were grown on the nanoridges, there was a striking localization of AP2-RFP on the ridge (Fig 1E). Thus, Ormocomp nanoridges provide a robust method to create regular, reproducible membrane curvature and to de-couple curvature generation from cell-intrinsic processes such as vesicle formation.

To determine the effect of the diameter of induced membrane curvature on the endocytic machinery, we seeded MDA-MB-231 cells, genome-edited to express fluorescent fusion proteins under endogenous regulatory control, on nanoridge substrates and imaged them on a TIRF microscope (Fig 2) (*15*). Imaging of plasma membrane markers showed that the entirety of the ventral plasma membrane is illuminated by the TIRF microscope (Fig 2A, Fig S1C, Fig S2A). The endocytic proteins demonstrated a striking preference for the higher-curvature ridges (e.g., 75, 120, and 200 nm) (Fig 2B-C), as reported previously for cells grown on quartz substrates (*6*). This observation was true of early-arriving endocytic proteins AP2 and clathrin light chain A (Fig 2B), as well as the intermediate curvature-generating protein epsin1 and late-peaking scission

GTPase dynamin2 (Fig 2C). The plasma membrane protein caveolin-1, which is not a component of CME sites, demonstrated no preferred binding to membranes of high curvature (Fig 2D).

To quantify the enrichment of endocytic sites on nanoridges with high curvature, we developed automated image processing tools. Using the bright field image of a cell on a substrate, we employed a line detection algorithm to create a mask that discriminates between on-and-off ridge sections of the cell. We next employed a Differences-of-Gaussians (DoG) algorithm to detect and localize fluorescent puncta. We corrected for increased cell membrane presence on nano-ridges by measuring the on-ridge increase in fluorescence of cell membrane markers BFP-Caax and CellMask Orange, which were in good agreement (Fig S2B). By measuring the relative abundance of endocytic proteins on the ridge vs flat membrane and dividing by the corrected area of the mask, we determined an enrichment score, which is a relative increase in likelihood of endocytic protein localization as a function of curvature.

The enrichment score demonstrates the strong preference of the endocytic machinery for regions of high plasma membrane curvature (Fig 2E). At the 75-nanometer ridge, AP2-RFP show a nearly 4-fold increase in puncta localization relative to flat membranes. Epsin1-GFP and dynamin2-GFP both show greater than a 4-fold enrichment. Swapping the fluorophores on AP2 and dynamin2 to GFP and RFP, respectively, resulted in little difference in enrichment (Fig S2C-D). These enrichments decrease with increasing diameter, until at the 500-nm ridge there is essentially no detectable enrichment. Clathrin light chain A, in contrast with other endocytic proteins, demonstrates a >3-fold enrichment at the smallest substrate size but precipitously decreases its enrichment as ridge size increases. This reduced enrichment may be because of the

presence of clathrin at other trafficking events within the cell body such as endosomes and the *trans*-Golgi network (*16*). These data demonstrate that CME proteins robustly reorganize across the cell in response to induced membrane curvature, with a strong preferential localization at highest induced positive curvature.

We next wondered whether the puncta of endocytic proteins present on curved membranes above nanoridges represent productive CCPs, TCALs, or ectopic protein localization (Fig 3). The ability to perform highly-sensitive TIRF imaging on nanoridge substrates allowed for precise quantitative analysis of fluorophore signal. To determine whether induced curvature promotes formation of productive endocytic sites, we imaged double-genome-edited MDA-MB-231 cells expressing AP2-TagRFP2 (herein called AP2RFP) and dynamin2-EGFP (herein DNM2GFP) at 0.5 Hertz on a range of ridge sizes. Kymographs and montages from two-color movies on flat Ormocomp substrates demonstrated the characteristic track of AP2RFP fluorescence accompanied by a burst of DNM2GFP fluorescence at the end of each AP2RFP track, a hallmark of productive endocytosis (Fig 3A-B) (*15*, *17*). Kymographs and montages from 75-, 120-, and 200-nanometer nano-ridges show the same stereotypical endocytic site behavior, indicating that the puncta present on nanoridges are productive CCPs (Fig 3A-B).

By using an established method of endocytic site detection and tracking, we measured the activity of the presumed CCPs over time in AP2RFP and DNM2GFP double-tagged cells (*17*). After event detection followed by binning to select for endocytic sites on induced curvature, we applied lifetime, MSD, and colocalization criteria according to previously published standards to select for valid CCPs (*15*, *17-18*). The lifetime of AP2 on flat substrates was 50.9+/-28s, similar to previously reported values for authentic CME sites on glass coverslips (*15*) (Fig 3C).

Endocytic sites on substrates with induced curvature followed the same pattern of AP2 increase followed by a dynamin2 peak, which marks productive vesicle scission, albeit with increased lifetimes of 58.4 +/- 30s for 75 nm ridges, 54.8 +/- 28 s for 120 nm ridges, and 53.5 +/- 29 for 200 nm ridges (Fig 3C-D). At diameters >200 nm, endocytic dynamics were unchanged by nanoridges (Fig S3A). This lifetime increase on smaller-diameter nanoridges is consistent with the finding that AP2 sites on collagen fibers have longer lifetimes than adjacent, non-collagen CCPs (*7*). Nanoridge-associated CCPs demonstrated increased spatial displacement during the last ten-second intervals of their lifetimes relative to CCPs budded from flat membranes (Fig 3E). The nanoridges did not change the percentages of transient, broken, incomplete, or persistent CCPs (Fig S3C).

In several cases of thin-section TEM we found CME vesicles budding from the side of a nano-ridge, as indicated by the spiked clathrin coat around the forming vesicle (Fig 3F) (*19*). We also found small, spiked coats on the tops of some ridges, suggesting that this is where the endocytic sites are initiated. These observations, combined with the increased displacement of nanoridge-CCPs before scission, lead us to hypothesize that endocytic sites preferentially form on sites of high positive curvature, then migrate from the top of the ridge to its side as the pit transitions to maturity and buds into the cell. The bulk rate of endocytosis, as measured by uptake of endocytic cargo transferrin tagged with Alexa-Fluor 647 (tfn-AF647), is not changed by the size of nanoridge (Fig S3D-E) (*20*).

TEM imaging of the 1000-nanometer substrate revealed a flat top with curved sides (Fig 1B, Fig S4A); cells grown on this size of ridge bear membrane curvature along the side of the ridge and flat membrane along the top of the ridge (Fig S4A). The diameter of the approximate semi-circle

on this curved edge of the ridge is ~210 nanometers, similar to that of the 120-nm nanoridge (Fig S4B). Consistent with the conclusion that substrate-induced membrane curvature recruits the endocytic machinery, AP2RFP preferentially appears at the edges of the 1000-nm ridges (Fig S4C). Indeed, a CCP can be seen by TEM protruding from the high-curvature edge (Fig S4A).

Induced curvature rescues endocytic protein recruitment upon clathrin knockdown

We hypothesized that the essential function of clathrin during CME might be to stabilize membrane curvature, and therefore that induced membrane curvature might bypass clathrin function (Fig 4A). Upon siRNA treatment, clathrin heavy chain (CLTC) expression was reduced by approximately 95%, as measured by western blot (Fig 4B). Previously, it was established that CME in mammalian cells is inhibited when clathrin is knocked down (*21-22*), leading to unstable nascent endocytic sites that stall as flat patches. Consistently, compared to sites seen in cells treated with control siRNA, clathrin knockdown on flat substrates leads to dimmer AP2RFP sites with markedly reduced DNM2GFP overlap, indicating that true endocytic sites are not formed (Fig 4C).

However, when clathrin knockdown cells were grown on nanoridges, there was a striking increase in AP2RFP intensity and apparent site size, and robust enrichment of dnm2GFP puncta at the sites of highest curvature was observed (Fig 4D). Thin-section TEM imaging revealed that the diameter of the membrane on nanoridges was unaffected by clathrin knockdown (Fig S5A-B). The enrichment score for AP2RFP and DNM2GFP was unchanged by clathrin siRNA, indicating that these early- and late-arriving CME proteins localize to sites of induced membrane curvature independent of clathrin (Fig 4E).

To test whether formation of curvature-dependent CME sites requires the adaptor protein AP2, we knocked down AP2 expression by siRNA and imaged cells on flat and curved substrates. Upon siRNA treatment, AP2 expression was depleted by >90%, as demonstrated by western blot and by a decrease in AP2 fluorescence in AP2RFP-tagged cells (Fig 4B, Fig S5C). AP2 disruption leads to a marked decrease in CLTARFP and DNM2GFP puncta that is not rescued by induced curvature (Fig 4 F-G). AP2-depleted cells on a flat substrate showed 3-fold decreased density of DNM2GFP puncta, and 2-fold decreased density of CLTARFP puncta (Fig 4H). Despite the diameter of induced membrane curvature being unchanged by AP2 siRNA (Fig S5A-B), the enrichment score for CLTARFP decreased significantly upon AP2 knockdown, from approximately 2.2 to 1.1 on 75nm substrates; this decrease in enrichment score is present across substrate sizes, indicating that clathrin is curvature-insensitive after AP2 disruption (Fig 4I). Cells treated with siRNA were illuminated to a depth of approximately 400 nanometers to ensure visualization of the entire ventral side of the cell, leading to an increase in visualization of endosomal or *trans*-Golgi associated CLTARFP puncta, which accounts for the apparent decrease in control-cell CLTARFP enrichment.

DNM2GFP puncta, however, were still 2-fold enriched on sites of high curvature, which is more modestly than in control cells (Fig 4I). This enrichment may be due to some innate curvature preference for dynamin2, or it may be due to dynamin2's roles in other endocytic pathways, which may be curvature-sensitive (*23*). These data indicate that curvature-induced endocytic sites depend on an AP2 function to precede endocytic patch stabilization, consistent with previous results (*7*, *22*).

Endocytic sites on curved substrates turn over and take up receptors despite clathrin disruption

Once we established that AP2 and dynamin2 localization in clathrin knockdown cells could be rescued by induced membrane curvature, we wondered whether these rescued sites turn over and take up cargo without the clathrin coat. To determine the kinetic profile for these sites over time, we recorded time-lapse TIRF microscopy of AP2/dynamin2 double-labeled cells after clathrin knockdown and tracked endocytic sites over time. We found that for cells treated with control siRNA, the sites of AP2/dynamin2 colocalization appeared as canonical endocytic sites, with a gradual increase in AP2 accompanied by a burst of dynamin2 to indicate scission (Fig 5A). Upon clathrin knockdown on flat substrates, the AP2 puncta were dimmer, small and unstable, with reduced dynamin2 co-localization. However, with substrate-stabilized 75 nm membrane curvature, the AP2 puncta became much larger and more stable; additionally, there was a burst of dynamin2 at a late stage of AP2 lifetime, followed by a decrease in AP2 fluorescence signal, hallmarks of CME vesicle scission. We found that the average lifetime of these tracks in clathrin knockdown cells (68+/-33s) was significantly increased over what was observed in control siRNA cells (50+/-26s), indicating that despite the normal appearance of the sites, their turnover is affected by clathrin knockdown (Fig 5B).

After binning the AP2/dynamin2 positive tracks according to lifetime, we found for cells grown on flat substrates that clathrin knockdown results in a decrease to only ~35% fluorescence signal for AP2/dynamin2 tracks relative to control siRNA (Fig 5C, left). The remaining dynamin2 signal showed a nearly symmetrical, noisy distribution over time, rather than a late-peaking recruitment characteristic of cells treated with control siRNA. However, tracks for cells grown

on 75nm substrates demonstrated a rescue of fluorescence intensity to ~70% of control, and the dynamin2 signal demonstrated the late peak characteristic of productive vesicle formation (Fig 5C, right).

Quantification of the overlap between AP2RFP tracks and DNM2GFP tracks on flat substrates versus curved ridges after clathrin knockdown demonstrates a dramatic rescue in overlap between the two fluorophores, from 29% overlap to 52%, matching the overlap with control siRNA (Fig 5D). In contrast, overlap between AP2GFP tracks and CLTARFP tracks was markedly decreased from 51% to 22%, and this decrease in fluorescence overlap is not changed by induced curvature, evidence that the rescue of the endocytic machinery is not provided by residual clathrin heavy chain.

We next sought to determine whether induced membrane curvature could also rescue cargo uptake in clathrin knockdown cells. We performed transferrin uptake assays with Alexa-Fluor 647-labeled transferrin (tfn-AF647). Upon exposure to media containing tfn-AF647, control siRNA-treated cells demonstrated perinuclear puncta of tfn-AF647, visible in X-Z protections (Fig 5E). In contrast, clathrin knockdown cells showed only membrane-associated tfn-AF647, which binds to its receptor but fails to be internalized. Clathrin knockdown cells with 75 nm of induced curvature, however, demonstrated a marked rescue of perinuclear tfn-AF647 puncta, indicating successful uptake of cargo. We measured the mean pixel intensity across control cells to be ~1200+/-500 AU (Fig 5F, Fig S5D). Clathrin knockdown cells on flat substrate had a mean pixel intensity of 69+/-22AU, while clathrin knockdown cells with 75nm of induced membrane curvature demonstrated a >3-fold increase in mean pixel intensity to 223+/-73 AU. The intensity of curvature-rescued cells is >4-fold weaker than control cells, which is consistent with 1)

exogenous curvature only partially rescuing endocytosis and 2) only ~⅓ of the cell, the ventral membrane contacting nanoridges, having induced membrane curvature. Through TEM imaging of clathrin knockdown cells, we found membrane-enclosed structures that lack a clear clathrin coat and have an elliptical shape, associated with the plasma membrane on induced curvature; these may represent vesicles near the time of scission produced through curvature-induced rescue of clathrin disruption (Fig S5E).

Finally, to test whether curvature could rescue cargo uptake in the absence of AP2, we repeated the transferrin uptake assay in the context of AP2 knockdown (Fig S5D). AP2 knockdown leads to membrane-associated tfn-AF647 signal, as the transferrin binds to its receptor on the plasma membrane but cannot cluster or be taken into the cell. AP2-knockdown cells grown on 75-nanometer ridges demonstrated tfn-AF647 evenly on the plasma membrane, and no puncta were visible over the diffuse membrane signal. The average pixel intensity in AP2-knockdown cells was not changed with statistical significance (Fig S5F). This result indicates that, within the sensitivity of our experiments, transferrin and/or its receptor itself are not curvature sensitive, and that CME protein preference for high membrane curvature is downstream of AP2 function.

Discussion

In this study, to gain insights into the feedback between membrane geometry and biochemical activity, we created induced nanoscale curvature in live cells. An attractive hypothesis for how curvature formation is controlled during vesicle formation is that membrane curvature itself acts as a signal to control biochemical reaction rates such as Bin-Amphiphysin-RVS domain protein recruitment, receptor clustering or lipid phosphatase activity (*24*). The UV-NIL approach

described here, with its ability to precisely control membrane curvature, coupled with quantitative cellular assays, will allow in vivo studies of many other curvature-sensitive proteins to more fully define how 3D nano-environment affects biochemical reaction rates underlying diverse cellular processes (*25*).

The factors that determine endocytic site localization in vivo are not fully known; while many cell types have pre-determined loci of preferred endocytosis, it is unclear how 3D, nanoscale context changes endocytic nucleation and stabilization. Our work and previous studies demonstrate that, all else being equal, endocytic site assembly is strongly biased to regions of high membrane curvature, as can be induced by rigid ECM fibers or by actin-based protrusions at adherens junctions, and that this curvature preference influences assembly of the earliest CME proteins, independent of the clathrin coat. This reaction to physical cues is expected to have significant downstream consequences in regulation of endocytic activity, as in mesenchymal migration or uptake of cadherins during the epithelial-to-mesenchymal transition (EMT) (*7*, *26*).

Curvature-induced CME, and the plasticity of clathrin coat dependence, may assist in divergent endocytosis such as viral uptake, as viral particles are orders of magnitude stiffer than the human plasma membrane and are often larger than canonical CCP cargoes (*27-28*). Upon clathrin disruption through siRNA, there is frequently a reduction—but not complete inhibition—of viral infectivity (*29-30*). Our evidence suggests that clathrin's key role in CME is to stabilize the membrane curvature that precedes vesicle uptake; by providing the necessary curvature to stabilize nascent AP2/cargo complexes absent clathrin, endocytic vesicle budding is possible with exogenous physical cues alone.

References and Notes

1. H. Suleiman, L. Zhang, R. Roth, J. E. Heuser, J. H. Miner, A. S. Shaw, A. Dani, Nanoscale protein architecture of the kidney glomerular basement membrane. *Elife*. 01149 (2013).

2. Z. Liu, J. L. Tan, D. M. Cohen, M. T. Yang, N. J. Sniadecki, A. Ruiz, C. M. Nelson, C. S. Chen, Mechanical tugging force regulates the size of cell-cell junctions. *Proc. Natl. Acad. Sci. U.S.A.* 0914547107 (2010)

3. J. E. Hassinger, G. Oster, D. G. Drubin, P. Rangamani, Design principles for robust vesiculation in clathrin-mediated endocytosis. *Proc. Natl. Acad. Sci. U.S.A.* 114(7) E1118-1127 (2017).

4. X. Tan, M. Luo, A. P. Liu, Clathrin-mediated endocytosis regulates fMLP-mediated neutrophil polarization. *Heliyon*. 4, e00819 (2018).

5. E. J. Ezratty, C. Bertaux, E. E. Marcantonio, G. G. Gundersen, Clathrin mediates integrin endocytosis for focal adhesion disassembly in migrating cells. *J. Cell Biol*. 187, 733–747 (2009).

6. W. Zhao, L. Hanson, H. Y. Lou, M. Akamatsu, P. D. Chowdary, F. Santoro, J. R. Marks, A. Grassart, D. G. Drubin, Y. Cui, B. Cui, Nanoscale manipulation of membrane curvature for probing endocytosis in live cells. *Nat. Nanotechnol*. 12, 750–756 (2017).

7. N. Elkhatib, E. Bresteau, F. Baschieri, A. L. Rioja, G. Van Niel, S. Vassilopoulos, G. Montagnac, Tubular clathrin/AP-2 lattices pinch collagen fibers to support 3D cell migration. *Science* 356, 6343 (2017)

8. L. Hinrichsen, A. Meyerholz, S. Groos, E. J. Ungewickell, Bending a membrane: How clathrin affects budding. *Proc. Natl. Acad. Sci. U. S. A*. 103, 8715–8720 (2006).

9. L. Von Kleist, W. Stahlschmidt, H. Bulut, K. Gromova, D. Puchkov, M. J. Robertson, K. A. Macgregor, N. Tomilin, A. Pechstein, N. Chau, M. Chircop, J. Sakoff, J. Peter Von Kries, W. Saenger, H.-G. Krä, O. Shupliakov, P. J. Robinson, A. Mccluskey, V. Haucke, Role of the Clathrin Terminal Domain in Regulating Coated Pit Dynamics Revealed by Small Molecule Inhibition. *Cell*. 146, 471–484 (2011).

10. O. Kovtun, V. K. Dickson, B. T. Kelly, D. J. Owen, J. A. G. Briggs, Architecture of the AP2/ clathrin coat on the membranes of clathrin-coated vesicles *Science Advances* 6(30) (2020).

11. D. Leyton-Puig, T. Isogai, E. Argenzio, B. Van Den Broek, J. Klarenbeek, H. Janssen, K. Jalink, M. Innocenti, Flat clathrin lattices are dynamic actin-controlled hubs for clathrin-mediated endocytosis and signalling of specific receptors. *Nat. Commun*. 8 (2017).

12. M. Bender, M. Otto, B. Hadam, B. Spangenberg, H. Kurz, in *Microelectronic Engineering* (Elsevier, 2002), vols. 61–62, pp. 407–413.

13. T. Gissibl, S. Wagner, J. Sykora, M. Schmid, H. Giessen, Refractive index measurements of photo-resists for three-dimensional direct laser writing. *Opt. Mater. Express*. 7, 2293 (2017).

14. P. B. Fischer, S. Y. Chou, Sub-50 nm high aspect-ratio silicon pillars, ridges and trenches fabricated using ultra-high E-beam lithography and RIE. *Conf. Solid State Devices Mater*. 1414, 443–445 (1992).

15. S. H. Hong, C. L. Cortesio, D. G. Drubin, Machine-Learning-Based Analysis in Genome-Edited Cells Reveals the Efficiency of Clathrin-Mediated Endocytosis. *Cell Rep*. 12, 2121–2130 (2015).

16. W. Stoorvogel, V. Oorschot, H. J. Geuze, A novel class of clathrin-coated vesicles budding from endosomes. *J. Cell Biol*. 132, 21–33 (1996).

17. F. Aguet, C. N. Antonescu, M. Mettlen, S. L. Schmid, G. Danuser, Advances in analysis of low signal-to-noise images link dynamin and AP2 to the functions of an endocytic checkpoint. *Dev. Cell*. 26, 279–291 (2013).

18. R. Pascolutti, V. Algisi, A. Conte, A. Raimondi, M. Pasham, S. Upadhyayula, R. Gaudin, T. Maritzen, E. Barbieri, G. Caldieri, C. Tordonato, S. Confalonieri, S. Freddi, M. G. Malabarba, E. Maspero, S. Polo, C. Tacchetti, V. Haucke, T. Kirchhausen, P. P. Di Fiore, S. Sigismund, Molecularly Distinct Clathrin-Coated Pits Differentially Impact EGFR Fate and Signaling. *Cell Rep*. 27, 3049-3061.e6 (2019).

19. T. F. Roth, K. R. Porter, Yolk Protein Uptake in the Oocyte of the Mosquito Aedes Aegypti. *J. Cell Biol*. 20, 313–332 (1964).

20. C. Harding, J. Heuser, P. Stahl, Receptor-mediated endocytosis of transferrin and recycling of the transferrin receptor in rat reticulocytes. *J. Cell Biol*. 97, 329–339 (1983).

21. L. Hinrichsen, J. Harborth, L. Andrees, K. Weber, E. J. Ungewickell, Effect of Clathrin Heavy Chain- and α-Adaptin-specific Small Inhibitory RNAs on Endocytic Accessory Proteins and Receptor Trafficking in HeLa Cells. *J. Biol. Chem*. 278, 45160–45170 (2003).

22. A. Motley, N. A. Bright, M. N. J. Seaman, M. S. Robinson, Clathrin-mediated endocytosis in AP-2-depleted cells. *J. Cell Biol*. 162, 909–918 (2003).

23. D. A. Schafer, S. A. Weed, D. Binns, A. V. Karginov, J. T. Parsons, J. A. Cooper, Dynamin2 and cortactin regulate actin assembly and filament organization. *Curr. Biol*. 12, 1852–1857 (2002).

24. J. Liu, Y. Sun, D. G. Drubin, G. F. Oster, The mechanochemistry of endocytosis. *PLoS Biol*. 7 , 1000204 (2009).

25. H. T. McMahon, J. L. Gallop, Membrane curvature and mechanisms of dynamic cell membrane remodelling. *Nature*. 438, 590-596 (2005).

26. E. Delva, A. P. Kowalczyk, Regulation of cadherin trafficking. *Traffic*. 10, 259–267 (2009).

27. M. G. Mateu, Mechanical properties of viruses analyzed by atomic force microscopy: A virological perspective. *Virus Res.* 168 (2012), pp. 1–22.

28. M. Ehrlich, W. Boll, A. Van Oijen, R. Hariharan, K. Chandran, M. L. Nibert, T. Kirchhausen, Endocytosis by random initiation and stabilization of clathrin-coated pits. *Cell*. 118, 591–605 (2004).

29. X. Sun, V. K. Yau, B. J. Briggs, G. R. Whittaker, Role of clathrin-mediated endocytosis during vesicular stomatitis virus entry into host cells. *Virology*. 338, 53–60 (2005).

30. Y. Inoue, N. Tanaka, Y. Tanaka, S. Inoue, K. Morita, M. Zhuang, T. Hattori, K. Sugamura, Clathrin-Dependent Entry of Severe Acute Respiratory Syndrome Coronavirus into Target Cells Expressing ACE2 with the Cytoplasmic Tail Deleted. *J. Virol*. 81, 8722–8729 (2007).

31. https://www.thermofisher.com/us/en/home/brands/product-brand/lipofectamine/lipofectamine-3000.html

32. J. Y. Tinevez, N. Perry, J. Schindelin, G. M. Hoopes, G. D. Reynolds, E. Laplantine, S. Y. Bednarek, S. L. Shorte, K. W. Eliceiri, TrackMate: An open and extensible platform for single-particle tracking. *Methods*. 115, 80–90 (2017).

33. https://docs.opencv.org/3.4/dd/d1a/group__imgproc__feature.html#ga46b4e588934f6c8dfd509cc6e0e4545a

Acknowledgments: We gratefully acknowledge Danielle Jorgens, Reena Zalpuri, and Guangwei Min of the UC Berkeley Electron Microscopy Lab for consultation and assistance in TEM and SEM imaging. Spinning-disk confocal imaging was conducted at the CRL Molecular Imaging Center, supported by the Gordon and Betty Moore Foundation. We also thank Stefano Cabrini, Scott Dhuey, Giuessepe Calafiore, and Stefano Dallorto of the Lawrence Berkeley Lab Molecular Foundry for assistance in silicon mold EBL/etching and Ormocomp substrate manufacturing, and Paul Lum of the UC Berkeley Biomoleuclar Nanotechnology Center for advice and assistance in Ormocomp lithography. Work at the Molecular Foundry was supported by the Office of Science, Office of Basic Energy Sciences, of the U.S. Department of Energy under Contract No. DE-AC02-05CH11231. We thank James Hurley and Leanna Owen of UC Berkeley and Ross Pedersen of the Carnegie Institute for comments on the manuscript.

Funding: National Institutes of Health grant R35GM118149 (DGD)

Author contributions:

Conceptualization: RCC, DGD

Methodology: RCC, CRS

Investigation: RCC

Visualization: RCC, CRS

Funding acquisition: DGD

Project administration: DGD

Supervision: DGD

Writing – original draft: RCC, DGD

Writing – review & editing: RCC, CRS, DGD

Competing interests: Authors declare no competing interests.

Data and materials availability: All data are available in the main and supplementary figures. Code for analysis can be found at github.com/drubinbarneslab.

Supplementary Materials

Materials and Methods

Figs. S1 to S5

References (*31–33*)

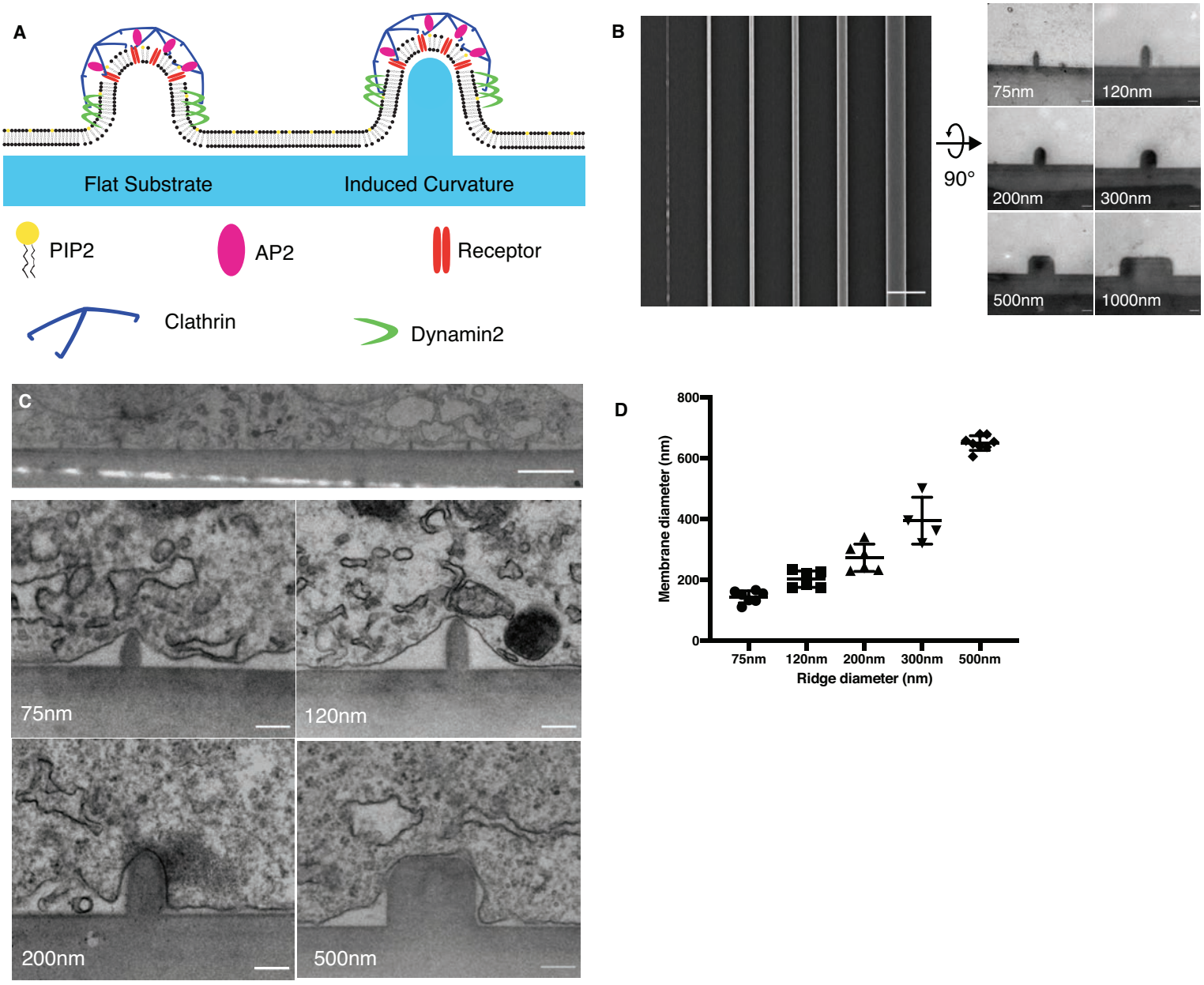
A
Flat Substrate
Induced Curvature
PIP2
AP2
Receptor
Clathrin
Dynamin2
B
90°
75nm
120nm
200nm
300nm
500nm
1000nm
C
75nm
120nm
200nm
500nm
D
Membrane diameter (nm)
800
600
400
200
0
75nm
120nm
200nm
300nm
500nm
Ridge diameter (nm)

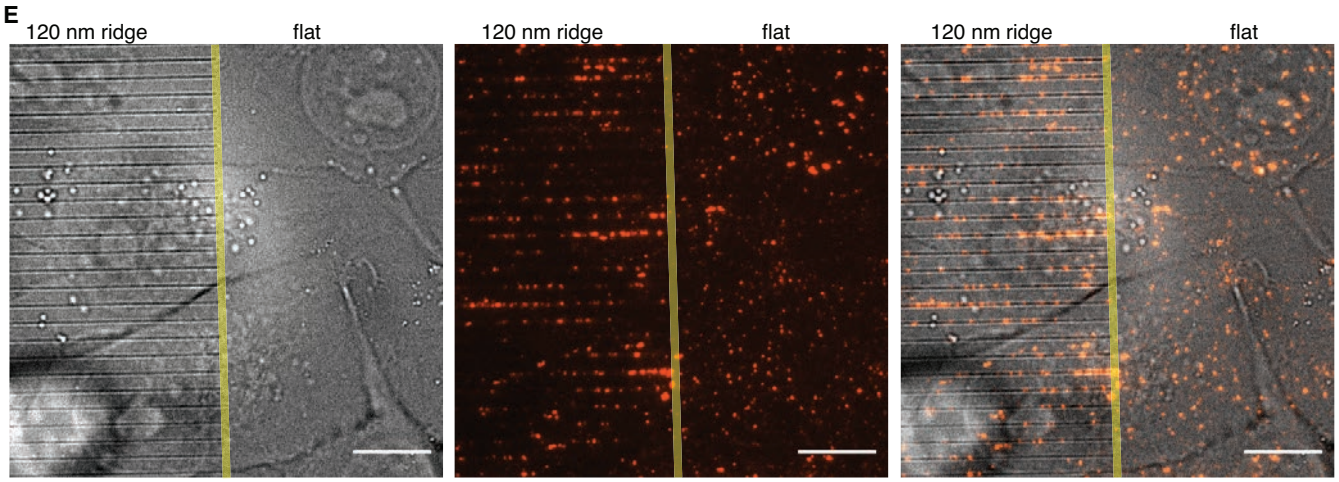
E
120 nm ridge
flat
120 nm ridge
flat
120 nm ridge
flat

Fig. 1. Ormocomp substrates induce nanometer-scale membrane curvature. (**A**) Induced curvature on the same size order as CCPs may stabilize the energetically-unfavorable U-shaped intermediate state of CME. (**B**) (Left) En-Face SEM of nanoridge substrates showing variable diameter of the ridge (scale bar 2 μM), and (right) thin-section TEM of nanoridges demonstrating the size and shape of nanoridges on which cells grow (scale bar 100 nm). (**C**) Thin-section TEM images of cells grown on nanoridges demonstrates the entire ventral membrane's response to induced curvature (scale bar 2 μM) as well as high-magnification images of cells bent around ridges of varying diameter with induced semi-circular membranes (scale bar 200nm). (**D**) Quantification of membrane diameter induced by nanoridges (Mean ± SD, $n \geq 4$ ridges from $n \geq 3$ cells). (**E**) TIRF/BF microscopy of live MDA-MB-231 cells grown on the edge of a nanoridge section demonstrates AP2 rearrangement in response to ridges (scale bar 10 μM).

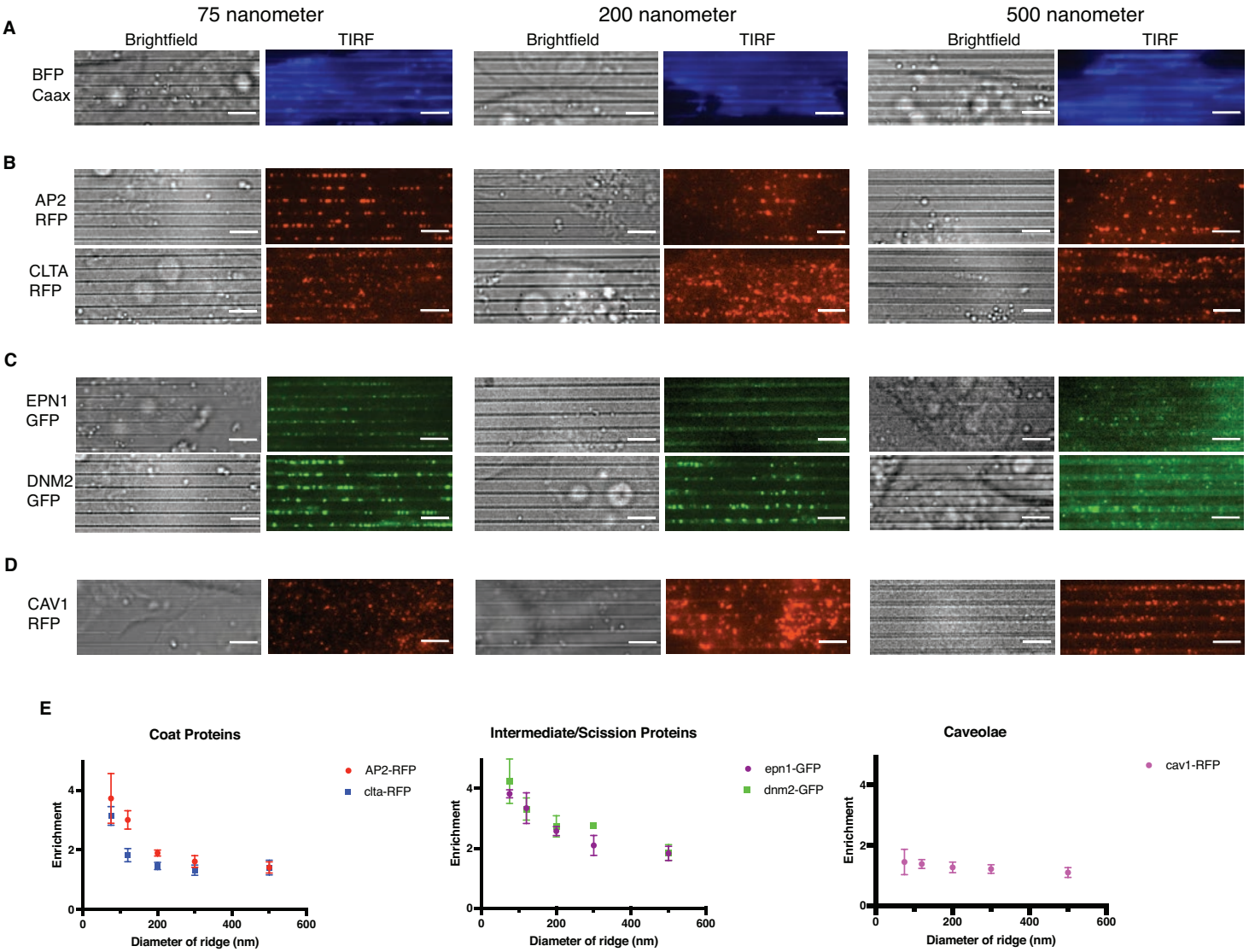

Fig. 2. Proteins from across CME respond to induced curvature as a function of radius. (**A**) TIRF microscopy of cell membrane marker BFP-Caax demonstrating even illumination across the ventral cell body. (**B-D)** Survey of endocytic proteins from across CME and caveolar endocytosis, imaged by TIRF microscopy, demonstrating strong CCP response to smallest-diameter curvature with weaker response to larger diameters. Caveolin-RFP shows no curvature preference (scale bars 4 μM). (**E**) Quantification of enrichment of endocytic proteins surveyed on ridges as a function of ridge diameter (Mean ± SD, $n \geq 5$ cells per condition).

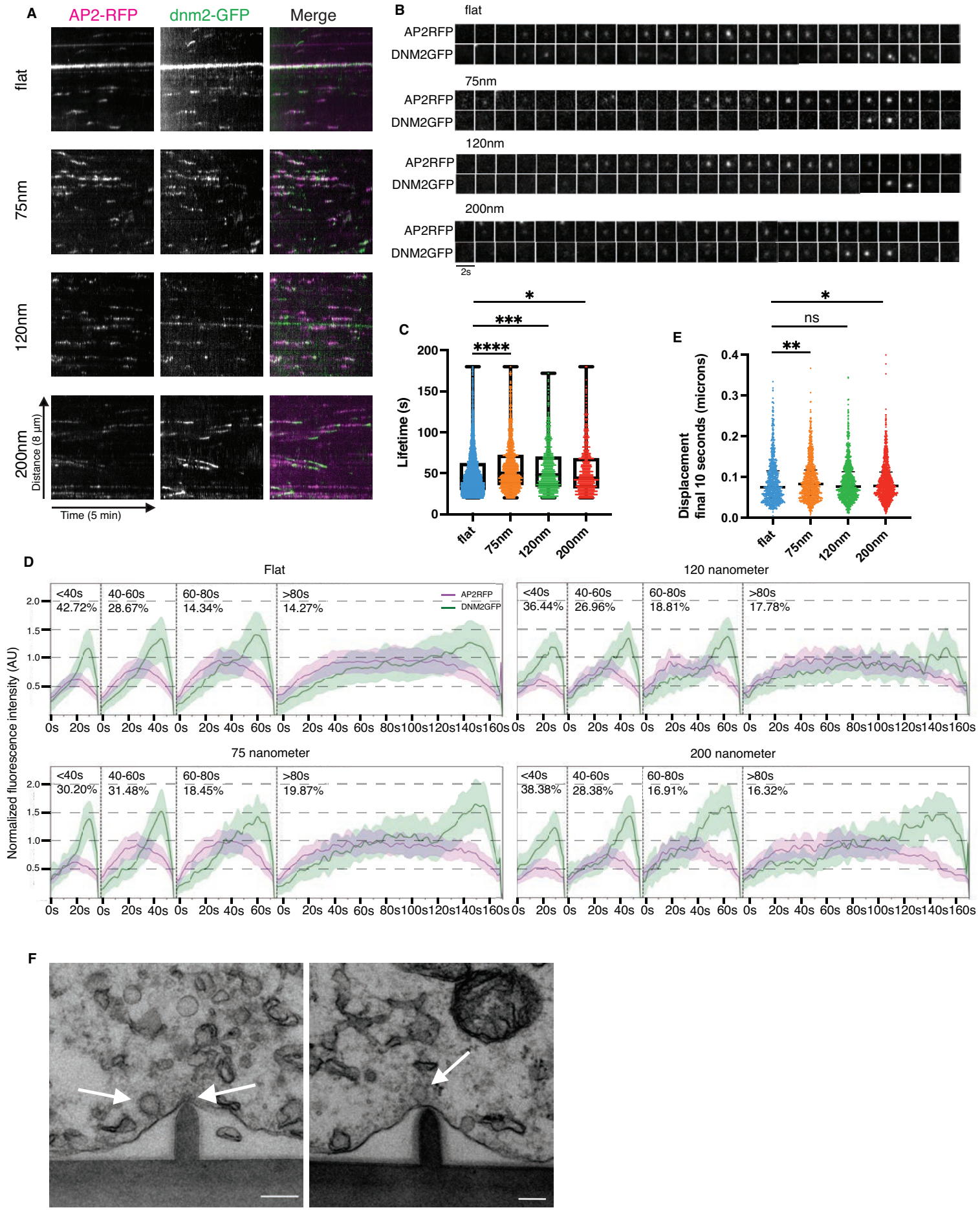
A
AP2-RFP
dnm2-GFP
Merge
flat
75nm
120nm
200nm
Distance (8 µm)
Time (5 min)
B
flat
75nm
120nm
200nm
AP2RFP
DNM2GFP
2s
C
Lifetime (s)
flat
75nm
120nm
200nm
E
Displacement final 10 seconds (microns)
ns
D
Flat
120 nanometer
75 nanometer
200 nanometer
AP2RFP
DNM2GFP
Normalized fluorescence intensity (AU)
<40s 42.72%
40-60s 28.67%
60-80s 14.34%
>80s 14.27%
<40s 36.44%
40-60s 26.96%
60-80s 18.81%
>80s 17.78%
<40s 30.20%
40-60s 31.48%
60-80s 18.45%
>80s 19.87%
<40s 38.38%
40-60s 28.38%
60-80s 16.91%
>80s 16.32%
F

Fig. 3. Endocytic protein localizations on nanoridges are bona fide CCPs with distinct kinetics. (**A-B**) Representative kymographs (**A**) and montages (**B**) from live TIRF microscopy of cells frown on flat and nanoridge substrates showing canonical pattern of AP2/dynamin2 fluorescence marking productive CCPs. (**C**) Lifetimes of CCPs as a function of curvature (Mean ± interquartile range, $n > 1000$ tracks from 4 cells per condition, *P* Student's t test). (**D**) CCP displacement in the final 10 seconds of an endocytic site lifetime as a function of curvature (Mean ± interquartile range, $n > 1000$ tracks from 4 cells per condition, *U* Mann-Whitney test). (**E**) Average normalized fluorescence intensity traces of AP2/dynamin2 for valid tracks from flat and nanoridge CCPs, binned according to lifetime. (**F**) Thin-section TEM of cells on nanoridge substrates with arrows marking coat protein atop ridge (left panel) and CCPs budding from sides of nanoridges (scale bar 100nm).

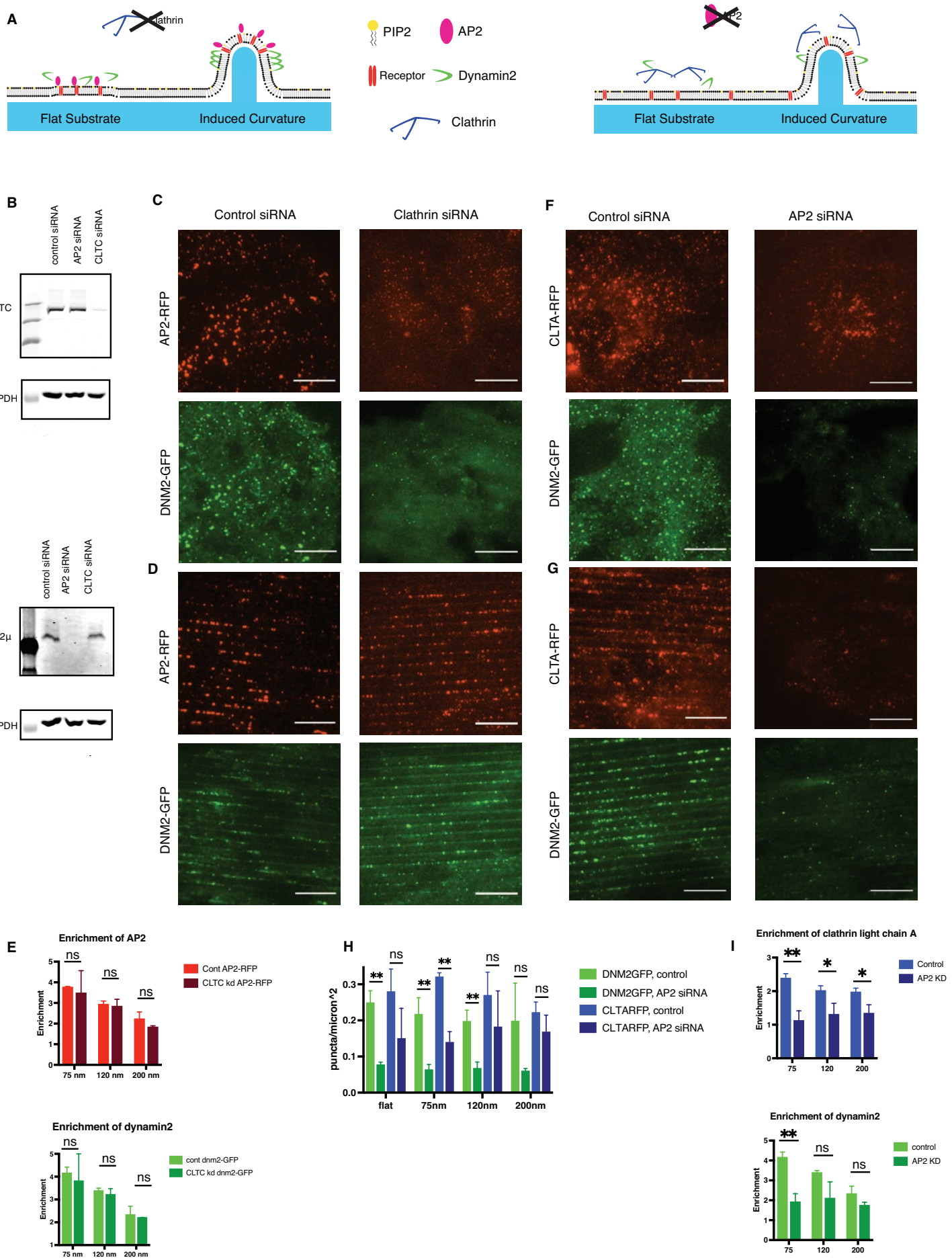
A
Clathrin
Flat Substrate
Induced Curvature
PIP2
AP2
Receptor
Dynamin2
Clathrin
AP2
Flat Substrate
Induced Curvature
B
control siRNA
AP2 siRNA
CLTC siRNA
CLTC
GAPDH
control siRNA
AP2 siRNA
CLTC siRNA
AP2µ
GAPDH
C
Control siRNA
Clathrin siRNA
AP2-RFP
DNM2-GFP
D
AP2-RFP
DNM2-GFP
F
Control siRNA
AP2 siRNA
CLTA-RFP
DNM2-GFP
G
CLTA-RFP
DNM2-GFP
E
Enrichment of AP2
Enrichment
ns
ns
ns
75 nm
120 nm
200 nm
Cont AP2-RFP
CLTC kd AP2-RFP
Enrichment of dynamin2
Enrichment
ns
ns
ns
75 nm
120 nm
200 nm
cont dnm2-GFP
CLTC kd dnm2-GFP
H
puncta/micron^2
**
ns
**
**
**
ns
ns
ns
flat
75nm
120nm
200nm
DNM2GFP, control
DNM2GFP, AP2 siRNA
CLTARFP, control
CLTARFP, AP2 siRNA
I
Enrichment of clathrin light chain A
Enrichment
**
*
*
75
120
200
Control
AP2 KD
Enrichment of dynamin2
Enrichment
**
ns
ns
75
120
200
control
AP2 KD

Fig. 4. Induced curvature rescues the localization of CCPs after clathrin knockdown but not AP2 knockdown. (**A**) Models of endocytic protein localization to flat or curved substrate with clathrin (left) or AP2 (right) disruption. (**B**) Western blots demonstrating depletion of clathrin heavy chain (top) or AP2μ subunit (bottom) 72 hours after transfection with siRNA. GAPDH was probed as a loading control. (**C**) Appearance of AP2/dnm2 proteins on flat substrate after clathrin knockdown imaged by TIRF microscopy. (**D**) Rescue of AP2 fluorescence intensity and dnm2 overlap for cells exposed to 75 nm induced curvature, imaged by TIRF microscopy. (**E**) Quantification of enrichment of AP2/dynamin2 on sites of curvature with control or clathrin siRNA (Mean ± SD, n = 3 cells per condition, P Student's t test). (**F**) Appearance of clathrin light chain-RFP and dynamin2-GFP upon AP2 knockdown and growth on flat substrate and (**G**) on 75nm induced curvature, imaged by TIRF microscopy. (**H**) Quantification of dynamin2 and clathrin light-chain A puncta with control or AP2 siRNA (Mean ±SD, n = 3 cells per condition, P Student's t test). (**I**) enrichment of remaining clathrin light chain A and dynamin2 puncta upon AP2 depletion (Mean ± SD, n = 3 conditions per cell, P Student's t test).

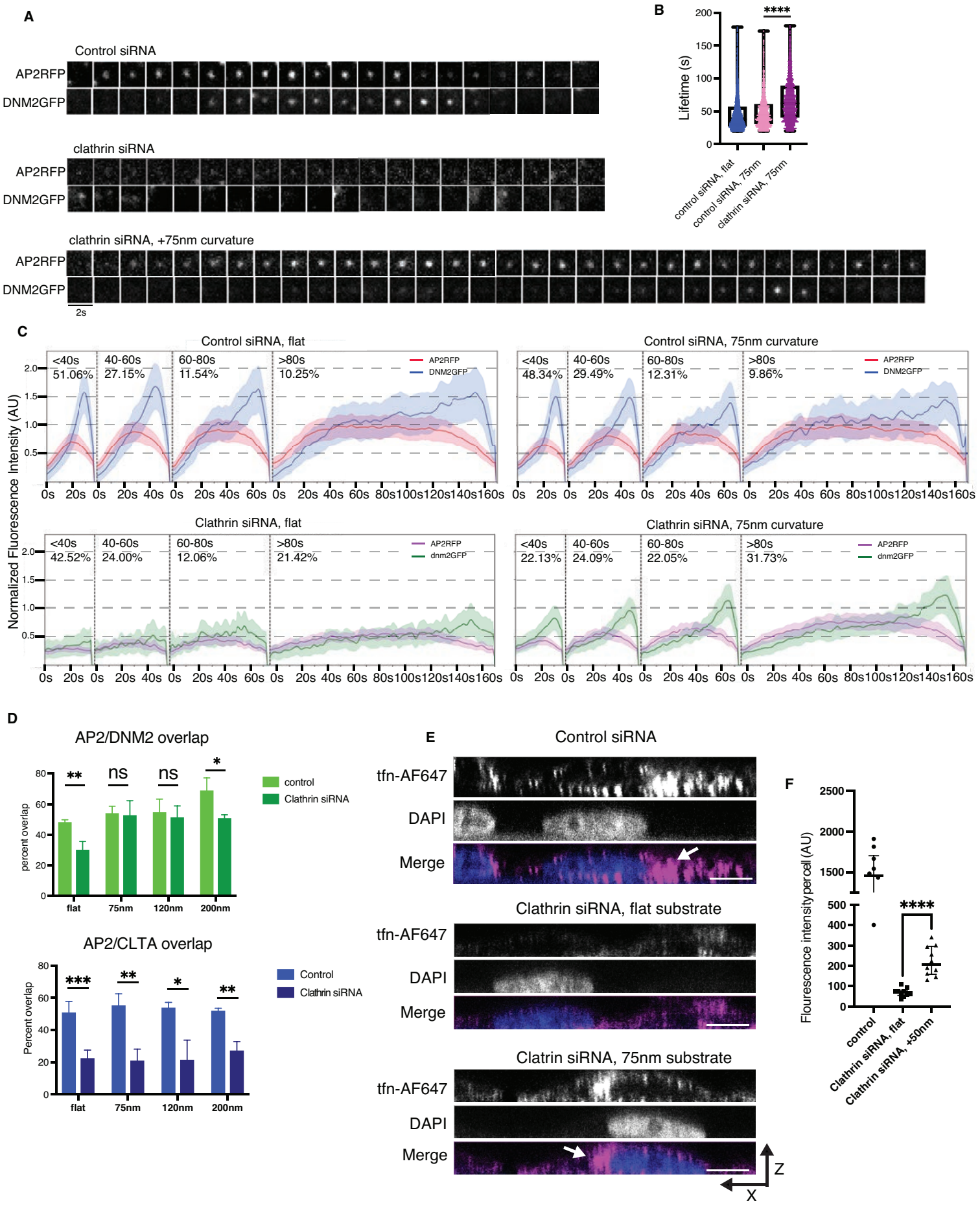
A
Control siRNA
AP2RFP
DNM2GFP
clathrin siRNA
AP2RFP
DNM2GFP
clathrin siRNA, +75nm curvature
AP2RFP
DNM2GFP
2s
B
****
Lifetime (s)
control siRNA, flat
control siRNA, 75nm
clathrin siRNA, 75nm
C
Control siRNA, flat
<40s 51.06%
40-60s 27.15%
60-80s 11.54%
>80s 10.25%
AP2RFP
DNM2GFP
Control siRNA, 75nm curvature
<40s 48.34%
40-60s 29.49%
60-80s 12.31%
>80s 9.86%
Clathrin siRNA, flat
<40s 42.52%
40-60s 24.00%
60-80s 12.06%
>80s 21.42%
dnm2GFP
Clathrin siRNA, 75nm curvature
<40s 22.13%
40-60s 24.09%
60-80s 22.05%
>80s 31.73%
Normalized Fluorescence Intensity (AU)
D
AP2/DNM2 overlap
percent overlap
control
Clathrin siRNA
flat
75nm
120nm
200nm
AP2/CLTA overlap
Percent overlap
Control
Clathrin siRNA
E
Control siRNA
tfn-AF647
DAPI
Merge
Clathrin siRNA, flat substrate
Clatrin siRNA, 75nm substrate
Z
X
F
Flourescence intensity per cell (AU)
control
Clathrin siRNA, flat
Clathrin siRNA, +50nm

Fig. 5. Curvature-rescued CCPs demonstrate turnover and increased transferrin uptake. (**A**) Representative montages of detected AP2/dynamin2 events from control and clathrin knockdown cells demonstrating rescue of canonical AP2/dynamin2 turnover even after clathrin knockdown with curvature. (**B**) Lifetimes of endocytic sites from control and clathrin siRNA CCPs. (Mean ± interquartile range, $n > 1000$ tracks per condition from 3-4 cells per condition P Student's t test). (**C**) Normalized fluorescence intensity of AP2/dynamin2 CCPs from flat (left) and 75-nm curvature (right) with control or clathrin siRNA. (**D**) Detected overlap of AP2/ dynamin2 or AP2/clathrin light chain upon clathrin heavy chain knockdown (Mean ± SD, $n = 3$ cells per condition, p Student's t test). (**E**) X-Z reconstructions of slices through the middle of cells after transferrin uptake assays from confocal microscopy of control siRNA and clathrin siRNA, with white arrows indicating perinuclear transferrin (scale bar 10 μM). (**F**) Quantification of transferrin fluorescence intensity per cell of clathrin siRNA-treated cells with or without induced curvature (Mean ± SD, $P < 0.0001$ Student's t test).